JSML
Journal of Science and Mathematics Letters
ISSN 2462-2052 • eISSN 2600-8718

Research Article

Heat Transfer Analysis on Thin Film Flow in MHD Ternary Nanofluid Over an Unsteady Stretching Sheet with Radiation Effect

Nur Syazana Anuar[1]*, Al-Nurul Amni Athirah Hasbullah[1], Nur Adilah Liyana Aladdin[2], Norfifah Bachok[3,4], Zeeshan Khan[5,6]

[1] Faculty of Computer and Mathematical Sciences, Universiti Teknologi MARA, 40450 Shah Alam, Selangor, Malaysia
[2] Department of Mathematics, Centre for Foundation Defence Studies, Universiti Pertahanan Nasional Malaysia, Kem Sg Besi, 57000 Kuala Lumpur, Malaysia
[3] Department of Mathematics and Statistics, Faculty of Science, Universiti Putra Malaysia, 43400 Serdang, Malaysia
[4] Institute for Mathematical Research, Universiti Putra Malaysia, 43400 UPM Serdang, Selangor, Malaysia
[5] School of Science, Harbin Institute of Technology, 518055, Shenzhen, China
[6] Department of Mathematics, Abdul Wali Khan University Mardan, 23200 Khyber Pakhtunkhwa, Pakistan
* Corresponding author: nursyazana931@uitm.edu.my

ARTICLE HISTORY

Received
14 November 2025
Revised
25 February 2026
Accepted
12 March 2026
Published
1 April 2026

KEYWORDS

Thin Film Flow
Response Surface Methodology
Radiation
Ternary Nanofluid

ABSTRACT

This study investigates heat transfer enhancement in a thin film flow over an unsteady stretching sheet by employing ternary nanofluids comprising three different nanoparticles suspended in water. Recognizing the limitations of conventional nanofluids, this research explores the synergistic effects of these nanoparticles to optimize heat transfer efficiency. Considering the significance of radiation in high-temperature applications, the study incorporates radiation heat transfer effects for accurate temperature predictions. Using similarity transformations, the governing equations are converted into a system of ordinary differential equations, which are then numerically resolved using Matlab's bvp4c solver. Response Surface Methodology (RSM) is used to examine the combined effects of radiation, magnetic fields, and nanoparticle composition on heat transfer properties in order to further improve heat transfer. By analyzing the impact of key parameters such as radiation, film thickness, nanoparticle volume fraction, suction/injection, magnetic field, and unsteadiness on skin friction, local Nusselt number, velocity, and temperature profiles, the study identifies optimal conditions for maximizing heat transfer efficiency. The findings suggest that thermal field of ternary nanofluid improves via radiation, stretching and Alumina nanoparticle parameters. Results also show that the optimized heat transfer involves a minimum Alumina nanoparticle parameter at the highest stretching and radiation parameters. This research provides valuable insights into the design and development of efficient thermal management systems in various applications, including aerospace, energy, and industrial sectors.

https://doi.org/10.37134/jsml.vol14.2.6.2026

1. INTRODUCTION

The movement of a liquid layer across a solid surface with a free boundary is known as thin film flow, and it is still a topic with significant scientific and engineering interest. From the simple production of dew to the intricate coating processes needed for the production of microelectronics, such flows can be found in a variety of natural and industrial processes (O'Brien & Schwartz, 2002). The unsteady flow of thin films made of hybrid nanoliquids under magnetic influence was studied by Malleswari and Sarojamma (2024), who found that magnetohydrodynamic (MHD) effects significantly impact heat transfer performance and velocity distribution. A comprehensive model for thin film heat transfer over an inclined spinning disk subjected to thermal radiation and viscous dissipation in hybrid nanofluids was created by Alharbi et al. (2024) in a related work. They proved that by carefully applying a porous material to thin film flows over an inclined spinning disc, heat transmission is significantly improved, leading to an increase in thermal efficiency.

The behavior of thin films with varying nanoparticle compositions was compared by Zeeshan et al. (2022), with an emphasis on copper (Cu) and aluminum oxide (AlO_3) in ethylene glycol base fluids. Their findings demonstrated that because copper has a higher density and thermal conductivity than aluminum oxide, thin films containing copper nanoparticles often generate smaller layers under the same flow circumstances. Platelet-shaped nanoparticles are the most effective for heat transfer, according to Gomathy and Kumar's (2024) investigation into the impact of nanoparticle morphologies on Ag-water nanofluid thin film flow through a porous media with thermal radiation and ohmic heating. More recently, Hayat et al. (2025) investigated the application of tetrahedron, hexahedron and lamina-shaped nanomaterials in thin film flow, showing that the hexahedron and lamina shaped Al_2O_3 nanoparticles produced the lowest and maximum heat transfer rates, respectively.

Significant progress has been made in a number of engineering domains as a result of the research of radiation parameters in boundary layer flows. By modifying surface parameters according to the radiation parameter, Mukhtar and Gul (2023) used radiation boundary layer theory to increase collector efficiency in solar thermal systems. Reddy et al. (2023) examined how MHD affected a Williamson nanofluid's flow across a porous material while taking thermal slippage, velocity, and radiation into account. The researchers discovered that radiation is essential for controlling the temperature of the boundary layer, which in turn influences the rates of heat transfer and the general thermal behavior. The relationship between heat radiation and viscous dissipation in magnetic FeO_4-ethylene glycol nanofluid flow across a declining surface was also examined by Reddy and Mangamma (2023) using numerical simulations, taking velocity slip effects and heat production into account.

The study of nanofluids, fluids whose thermophysical characteristics are improved by the dispersion of nanoparticles in base liquids like water, kerosene, ethylene glycol, and motor oil has become a popular field of study. The flow behavior of ternary hybrid nanofluids has been studied by a number of researchers due to its significance in industrial applications. Compared to traditional nanofluids, these fluids constitute a more complex system since they comprise suspensions of three distinct kinds of nanoparticles in a base fluid. Alraddadi et al. (2023) used three different nanoparticles to conduct a mathematical investigation of cross bio-nanofluid flow around a stagnation point. According to Jamrus et al. (2024a), increasing the concentration of titania enhanced the efficiency of heat transfer in a Cu-Al_2O_3-TiO_2/water nanofluid model. Furthermore, ternary hybrid nanofluids like Cu–Al_2O_3–TiO_2 showed higher skin friction and heat transfer coefficients than binary hybrid nanofluids like Cu–Al_2O_3, according to an analysis of dual solutions for ternary hybrid nanofluid Hiemenz flow over a decreasing surface by Jamrus et al. (2024b), Hema et al. (2025), Haq et al. (2025), and Ramesh et al. (2025) further provided more evidence of the effectiveness of ternary nanofluid flows in a variety of physical settings.

For many engineering applications, such as thermal management, energy systems, and industrial processes, improving heat transfer in boundary layer flows is essential. Through a methodical analysis of the effects of several input parameters, Response Surface Methodology (RSM) has shown itself to be a successful strategy for optimizing heat transfer performance. The MHD convective flow of Carreau nanofluids was studied by Mathew et al. (2021) using RSM and sensitivity analysis, with an emphasis on the effects of slip conditions, chemical processes, and linear radiation. In order to maximize the heat transfer rate of Homann's stagnation-point flow of nanofluids across a diminishing surface, Wahid et al. (2024) used RSM. RSM was utilized more recently by Samat et al. (2024) to maximize heat transport in hybrid carbon nanotube-based nonlinear stretching/shrinking sheets. To solve energy-related problems, a number of other researchers have also used statistical optimization through RSM (Gull et al., 2024; Pyari et al., 2025; Wahid et al., 2025).

To the author's knowledge and according to the listed sources, no previous research has examined the importance of radiation impacts in the thin film flow of ternary nanofluids. Additionally, this research utilizes Response Surface Methodology (RSM) with the Central Composite Design (CCD)

model to enhance the heat transfer rate by methodically examining the effects of radiation, stretching rate, and nanoparticle volume percentage. This study addresses a critical deficiency in the existing literature and establishes a foundation for subsequent research focused on enhancing the efficiency and performance of ternary nanofluid applications in many engineering domains, especially in the optimization of heat transfer.

2. METHODOLOGY

2.1. Mathematical Modeling

Consider an unsteady two-dimensional electrically conducting thin liquid flow over a stretching surface, accounting for the effects of radiation as shown in Figure 1. The rectangular coordinates (x,y) are chosen to ensure that the stretching sheet is aligned at $y=0$, which means that the $x-$axis is on the extending surface and the $y-$axis is orthogonal to the sheet. A uniform magnetic field, $B(t)=B_0(1-\alpha t)^{-1/2}$ which varies with time, t is applied perpendicular to the sheet. It is assumed that the flow is laminar and that both the base fluid and the nanoparticles are in thermal equilibrium.

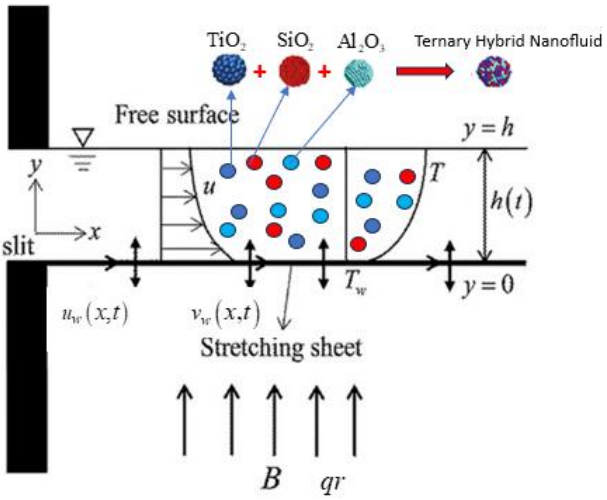

Figure 1. Schematic Diagram

The governing equations for the flow of thin films are the continuity, momentum and energy equations. The boundary layer form of these governing equations is presented as follows (Kamis et al., (2022):

$$\frac{\partial u}{\partial x}+\frac{\partial v}{\partial y}=0 \tag{1}$$

$$\frac{\partial u}{\partial t}+u\frac{\partial u}{\partial x}+v\frac{\partial u}{\partial y}=\frac{\mu_{thnf}}{\rho_{thnf}}\frac{\partial^2 u}{\partial y^2}-\frac{\sigma_{thnf}}{\rho_{thnf}}B^2(t)u \tag{2}$$

$$\frac{\partial T}{\partial t}+u\frac{\partial T}{\partial x}+v\frac{\partial T}{\partial y}=\frac{k_{thnf}}{\left(\rho C_p\right)_{thnf}}\frac{\partial^2 T}{\partial y^2}+\frac{1}{\left(\rho C_p\right)_{thnf}}\frac{\partial q_r}{\partial y} \tag{3}$$

with boundary conditions

$$\begin{aligned} &y=0: \quad u=u_w, \quad v=v_w, \quad T=T_w \\ &y=h: \quad \frac{\partial u}{\partial y}=\frac{\partial T}{\partial y}=0, \quad v=\frac{dh}{dt} \end{aligned} \tag{4}$$

where u and v represented the main velocity phenomena on the $x-$ and $y-$axes, respectively, T is the temperature and subscript term *thnf* is for the ternary nanofluid.

It is presumed that the stretching sheet, which generates the flow along the $x-$axis with velocity $u_w=cx/(1-\alpha t)$, is responsible for the flow over a thin film with thickness $h(t)$, where c and α are

constant. When developing the model, one of the boundary layer controllers, which is known as the mass velocity $v_w = v_0/(1-\alpha t)^{1/2}$, is considered. While the thin film's temperature varies in the manner described below:

$$T_w = T_0 - T_{ref}\left(\frac{bx^2}{2\nu_f}\right)(1-\alpha t)^{-3/2} \tag{5}$$

where v_0 corresponds to the initial velocity of suction/injection parameter, T_0 and T_{ref} are the variable slit temperature and temperature at the reference for all $t < 1/\alpha$. The Rosseland approximation is employed to account for solar radiation effects, therefore the radiative heat flux q_r is defined as:

$$q_r = \frac{16\sigma^* T_0^3}{3k^*}\left(\frac{\partial T}{\partial y}\right)_{y=0} \tag{6}$$

where k^* signifies the mean absorption and σ^* be the constant of Stefan-Boltzmann. The thermophysical properties, including dynamic viscosity μ, density ρ, heat capacity ρC_p, electrical conductivity σ, and thermal conductivity k are schematically presented in Table 1.

Table 1. Thermophysical Properties of Ternary Nanofluid (Bilal et al. (2022))

Thermophysical Properties	Ternary Nanofluid
Dynamic Viscosity	$\mu_{thnf} = \dfrac{\mu_f}{(1-\phi_1)^{2.5}(1-\phi_2)^{2.5}(1-\phi_3)^{2.5}}$
Density	$\rho_{thnf} = (1-\phi_1)\left\{(1-\phi_2)\left[(1-\phi_3)\rho_f + \phi_3\rho_3\right] + \phi_2\rho_2\right\} + \phi_1\rho_1$
Heat Capacity	$(\rho C_p)_{thnf} = (1-\phi_1)\left\{(1-\phi_2)\left[(1-\phi_3)(\rho C_p)_f + \phi_3(\rho C_p)_3\right] + \phi_2(\rho C_p)_2\right\} + \phi_1(\rho C_p)_1$
Electrical Conductivity	$\dfrac{\sigma_{thnf}}{\sigma_{hnf}} = \dfrac{(1+2\phi_1)\sigma_1 + (1-2\phi_1)\sigma_{hnf}}{(1-\phi_1)\sigma_1 + (1+\phi_1)\sigma_{hnf}}$
	where $\dfrac{\sigma_{hnf}}{\sigma_{nf}} = \dfrac{(1+2\phi_2)\sigma_2 + (1-2\phi_2)\sigma_{nf}}{(1-\phi_2)\sigma_2 + (1+\phi_2)\sigma_{nf}}$ and $\dfrac{\sigma_{nf}}{\sigma_f} = \dfrac{(1+2\phi_3)\sigma_3 + (1-2\phi_3)\sigma_f}{(1-\phi_3)\sigma_3 + (1+\phi_3)\sigma_f}$
Thermal Conductivity	$\dfrac{k_{thnf}}{k_{hnf}} = \dfrac{k_1 + 2k_{hnf} - 2\phi_1(k_{hnf} - k_1)}{k_1 + 2k_{hnf} + \phi_1(k_{hnf} - k_1)}$
	where $\dfrac{k_{hnf}}{k_{nf}} = \dfrac{k_2 + 2k_{nf} - 2\phi_2(k_{nf} - k_2)}{k_2 + 2k_{nf} + \phi_2(k_{nf} - k_2)}$ and $\dfrac{k_{nf}}{k_f} = \dfrac{k_3 + 2k_f - 2\phi_3(k_f - k_3)}{k_3 + 2k_f + \phi_3(k_f - k_3)}$

Here, the subscript term hnf, nf and f are for the hybrid nanofluid, nanofluid and base fluid, respectively, where 1, 2 and 3 stand for different type of particles. Meanwhile, ϕ_1, ϕ_2 and ϕ_3 represents the solid volume fraction of Titanium dioxide (TiO_2), Silicon dioxide (SiO_2) and Alumina (Al_2O_3), respectively. Table 2 illustrates the designated values of the proposed nanoparticles and base fluid.

Table 2. Thermophysical Properties of Nanoparticles and base fluid (Puneeth et al. (2021), Sharma et al. (2023))

Properties	H_2O	TiO_2	SiO_2	Al_2O_3
$\rho(kg/m^3)$	997.1	4250	2270	6310
$\sigma(S/m)$	5.5×10^{-6}	2.4×10^{6}	3.5×10^{6}	5.96×10^{7}
$k(W/\,mK)$	0.613	8.953	1.4013	32.9
$C_p(J/\,kgK)$	4179	711	730	686.2

To simplify the analysis, a stream function ψ is introduced, such that $u = \partial\psi/\partial y$ and $v = -\partial\psi/\partial x$. Additionally, an appropriate similarity transformation is given by:

$$\psi = \left[\nu_f b(1-\alpha t)^{-1}\right]^{\frac{1}{2}} x\zeta f(\eta), \quad T = T_0 - T_{ref}\left(\frac{bx^2}{2\nu_f}\right)(1-\alpha t)^{-\frac{3}{2}}\theta(\eta), \quad \eta = \left(\frac{\nu_f}{b}\right)(1-\alpha t)^{-\frac{1}{2}}\zeta^{-1}y \tag{7}$$

where θ and f represents the dimensionless temperature and velocity, respectively. ζ is the dimensionless thickness of the film, defined as (Wang (1990)):

$$\zeta = \left[\frac{b}{\nu_f(1-\alpha t)}\right]^{1/2} h \tag{8}$$

The transformations introduced in Equation (7) are applied in Equations (1) to (4). Equation (1) is proven identically, and Equations (2) to (4) are derived in the following forms:

$$\frac{\mu_{thnf}/\mu_f}{\rho_{thnf}/\rho_f} f''' + \lambda\left[ff'' - f'^2 - S\left(f' + \frac{1}{2}\eta f''\right) - \frac{\sigma_{thnf}/\sigma_f}{\rho_{thnf}/\rho_f} Mf'\right] = 0 \tag{9}$$

$$\frac{1}{\Pr}\left[\frac{k_{thnf}/k_f}{\left(\rho C_p\right)_{thnf}/\left(\rho C_p\right)_f} + \frac{4}{3}\frac{Rd}{\left(\rho C_p\right)_{thnf}/\left(\rho C_p\right)_f}\right]\theta'' + \lambda\left[f\theta' - 2f'\theta - \frac{S}{2}\left(3\theta + \eta\theta'\right)\right] = 0 \tag{10}$$

The boundary conditions that have been established are as follows:

$$\begin{aligned} &f(0) = w, \quad f'(0) = \varepsilon, \quad \theta(0) = 1, \\ &f''(1) = 0, \quad f(1) = \frac{S}{2}, \quad \theta'(1) = 0 \end{aligned} \tag{11}$$

It is noteworthy that prime denotes differentiation with respect to η. The generated non-dimensional parameter such as thin film thickness λ, unsteady parameter S, magnetic parameter M, radiation parameter Rd, suction/injection parameter w, stretching parameter $\varepsilon(\geq 0)$ and Prandtl number Pr are as follows:

$$\lambda = \zeta^2, \quad S = \frac{\alpha}{b}, \quad M = \frac{B_0^2\sigma_f}{\rho_f b}, \quad Rd = \frac{4\sigma^* T_0^3}{k^* k_f}, \quad w = -\frac{v_0}{\zeta\sqrt{\nu_f b}}, \quad \varepsilon = \frac{c}{b}, \quad \Pr = \frac{\left(C_p\mu\right)_f}{k_f} \tag{12}$$

The skin friction coefficient C_f and the local Nusselt number Nu_x are:

$$C_f = \frac{\mu_{thnf}\left(\frac{\partial u}{\partial y}\right)_{y=0}}{\rho_f u_w^{\,2}}, \qquad Nu_x = \frac{-x\left(k_{thnf} + \frac{16\sigma^* T_0^3}{3k^*}\right)\left(\frac{\partial T}{\partial y}\right)_{y=0}}{k_f\left(T_w - T_0\right)} \tag{13}$$

Substituting Equation (7) into (13), the quantities of the reduced skin friction and local Nusselt are:

$$C_f \,\mathrm{Re}_x^{1/2} = \frac{1}{\zeta}\frac{\mu_{thnf}}{\mu_f} f''(0), \quad Nu_x \,\mathrm{Re}_x^{-\frac{1}{2}} = -\frac{1}{\zeta}\left(\frac{k_{thnf}}{k_f} + \frac{4}{3}Rd\right)\theta'(0) \tag{14}$$

where $\mathrm{Re}_x = xu_w/\nu_f$ is the local Reynold number.

2.2. Response Surface Methodology

Response surface methodology consists of a family of mathematical and statistical techniques developed to build empirical predictive models for optimization (Montgomery (2017)). RSM is one of the powerful tools for understanding and optimizing local Nusselt number for a large number of applications in heat transfer. The application of RSM for optimizing this parameter will enable researchers to enhance heat transfer efficiency in different systems like heat exchangers, electronic cooling systems, combustion chambers, and thermal management devices (Bhattacharya et al. (2002). The following three independent variables were selected for the study: (i) Alumina nanoparticle volume fraction ϕ_3, (ii) stretching rate ε and (iii) radiation Rd. Each of the variables had three levels of definition and such that: low or minimum (represented by -1), medium-central (represented by 0), and high or maximum (represented by +1). A central composite design (CCD) was employed to assess how key factors influence the local Nusselt number. The experimental design comprised twenty (20) test runs, including six (6) central points, and evaluated three critical independent variables to optimize their effect on the local Nusselt number response. Table 3 shows the operating levels and ranges of independent variables evaluated in the present study while Table 4 displays the outcomes of these runs.

Table 3. Different levels of values of independent variables (factors)

Factors	Coded symbol	Low level (-1)	Medium level (0)	High level (1)
ϕ_3	x_1	0.005	0.01	0.015
ε	x_2	1	1.5	2
Rd	x_3	0.2	0.4	0.6

Table 4. Response result regarding RSM design when $\phi_1 = \phi_2 = 0.01$, $S = 0.8$, $M = 0.2$ and $w = 0.2$

Run	ϕ_3	ε	Rd	x_1	x_2	x_3	Response ($Nu_x \mathrm{Re}_x^{-1/2}$)	ζ
1	0.005	1	0.2	-1	-1	-1	7.4924716	3.3239529
2	0.015	1	0.2	1	-1	-1	7.5088592	3.2897179
3	0.005	2	0.2	-1	1	-1	10.2850356	4.8831497
4	0.015	2	0.2	1	1	-1	10.2954146	4.8310808
5	0.005	1	0.6	-1	-1	1	8.2829327	3.3239529
6	0.015	1	0.6	1	-1	1	8.2913154	3.2897179
7	0.005	2	0.6	-1	1	1	11.2768434	4.8831497
8	0.015	2	0.6	1	1	1	11.2763575	4.8310808
9	0.005	1.5	0.4	-1	0	0	9.4747808	4.1871945
10	0.015	1.5	0.4	1	0	0	9.4822527	4.1431325
11	0.01	1	0.4	0	-1	0	7.9107124	3.3063131
12	0.01	2	0.4	0	1	0	10.8052143	4.8563153
13	0.01	1.5	0.2	0	0	-1	9.0123076	4.1644884
14	0.01	1.5	0.6	0	0	1	9.9030332	4.1644884
15	0.01	1.5	0.4	0	0	0	9.4778060	4.1644884
16	0.01	1.5	0.4	0	0	0	9.4778060	4.1644884
17	0.01	1.5	0.4	0	0	0	9.4778060	4.1644884
18	0.01	1.5	0.4	0	0	0	9.4778060	4.1644884
19	0.01	1.5	0.4	0	0	0	9.4778060	4.1644884
20	0.01	1.5	0.4	0	0	0	9.4778060	4.1644884

In the optimization process, responses can be directly correlated to the selected factors through either linear or quadratic models. The quadratic model, which encompasses the linear model, is expressed as:

$$Y = r_0 + r_1 x_1 + r_2 x_2 + r_3 x_3 + r_{11} x_1^2 + r_{22} x_2^2 + r_{33} x_3^2 + r_{12} x_1 x_2 + r_{23} x_2 x_3 + r_{13} x_1 x_3 \tag{15}$$

The response surface Equation (15) contains one intercept term (r_0), three linear coefficients (r_1, r_2, r_3) three quadratic terms (r_{11}, r_{22}, r_{33}), and three interaction coefficients (r_{12}, r_{23}, r_{13}).

3. RESULTS AND DISCUSSION

3.1. Validation

The Matlab software's bvp4c function was used to numerically solve the system of Ordinary Differential Equations (8)-(10). The Prandtl number is set equal to 6.2 for the entire computation which indicates water as a base fluid. Prior to employing the proposed numerical technique to solve the current problem, a code validation was conducted with Wang (2006) (Homotopy analysis method), Noor et al. (2010) (Homotopy analysis method) and Das et al. (2017) (Nachtsheim and Swigert shooting iteration technique together with Runge-Kutta sixth-order integration scheme) when $\varepsilon = 1$ (stretching case) $\phi_1 = \phi_2 = \phi_3 = 0$ (pure water), $w = 0$ (impermeable) and $M = Rd = 0$. Tables 5 and 6 show that the results obtained for skin friction coefficient $-f''(0)$, free surface temperature $\theta(1)$ and the rate of heat transfer $-\theta'(0)$ are in good agreement.

Table 5. Skin friction coefficient $-f''(0)$ for various unsteady parameter S when $\mathrm{Pr} = 1$

S	Wang (2006)		Das *et al.* (2017)		Present	
	ζ	$-f''(0)$	ζ	$-f''(0)$	ζ	$-f''(0)$
0.8	2.15199	2.68094	2.151994	2.6809430214	2.1519937	2.680965615
1.0	1.54362	1.97238	1.543626	1.9723777720	1.5436161	1.972384883
1.2	1.127780	1.442631	1.127780	1.4444265502	1.1277809	1.442625189
1.4	0.821032	1.012784	0.821055	1.0127845562	0.8210322	1.012780168
1.6	0.567173	0.642397	0.576173	0.6423988882	0.5761730	0.642396990

Table 6. Free surface temperature $\theta(1)$ and rate of heat transfer $-\theta'(0)$ for various Prandtl number Pr

Pr	Wang (2006)		Noor et al. (2010)		Present	
	$\theta(1)$	$-\theta'(0)$	$\theta(1)$	$-\theta'(0)$	$\theta(1)$	$-\theta'(0)$
			$S=0.8(\zeta=2.1519937)$			
1	0.097884	3.595970	0.097881	3.593268	0.0978842	3.595991096
2	0.024941	5.244150	0.024945	5.226744	0.0248625	5.259186877
3	0.008785	6.514440	0.008786	6.382744	0.0083111	6.533702085
			$S=1.2(\zeta=1.1277809)$			
1	0.286717	1.999590	0.286712	1.999224	0.286717	1.999591724
2	0.128124	2.975450	0.128031	2.975320	0.128121	2.975905708
3	0.067658	3.698830	0.067423	3.693560	0.067645	3.701320136

3.2. Profiles and Physical Quantities

In the current problem, a critical parameter is the layer thickness. Currently, the boundary layer flow depends on the thin film thickness parameter ζ. Figures 2(a)-(b) illustrate how Alumina nanoparticle volume fraction ϕ_3 affects the velocity $f'(\eta)$ and temperature $\theta(\eta)$ profiles when $w=0.2$ (suction case) and $w=-0.2$ (injection case). The velocity profile in Figure 2(a) decreases as ϕ_3 increases, suggesting a higher resistance to flow. The thin film thickness ζ also decreases, and suction $(w=0.2)$ results in greater velocities near the boundary than injection $(w=-0.2)$. The heat capacitance of the ternary nanofluid increases as the Alumina solid volume fraction ϕ_3 increases, resulting in the fluid storing more heat and a decrease in its temperature, as illustrated in Figure 2(b). The reduction in film thickness ζ, along with the rise in nanoparticle volume fraction ϕ_3, is resulting in an elevation of the fluid's heat capacity, hence decreasing the fluid's temperature. The temperature gradient closes the wall is observed to be steeper due to the suction, compared to the injection.

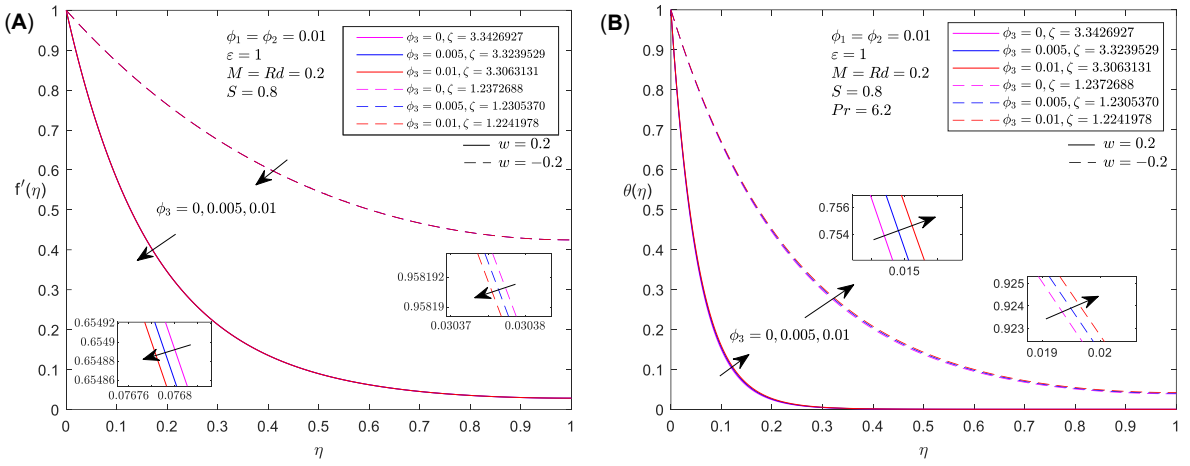

Figure 2. Variation in velocity (**A**) and temperature (**B**) profiles for different Alumina nanoparticle ϕ_3

The effects of S (unsteady parameter) on the resulting velocity $f'(\eta)$ and temperature $\theta(\eta)$ profiles are visualized in Figure 3(a)-(b). Higher values of the unsteadiness parameter S imply more unstable flow, which can result in decreased velocity and temperature. This occurs because increased unsteadiness causes stronger deceleration or instability in the flow, resulting in decreased velocity. Furthermore, the increased unsteadiness could hinder heat transmission or influence the thermal boundary layer, resulting in a lower fluid temperature. A decrease in the thin film thickness ζ of the boundary layer is observed as the unsteadiness parameter S increases. The natural formation and development of the boundary layer are disrupted by this increased unsteadiness. Specifically, the boundary layer is unable to fully develop as anticipated in a stable or less unsteady flow regime due to the increased fluctuations and instabilities associated with elevated S values.

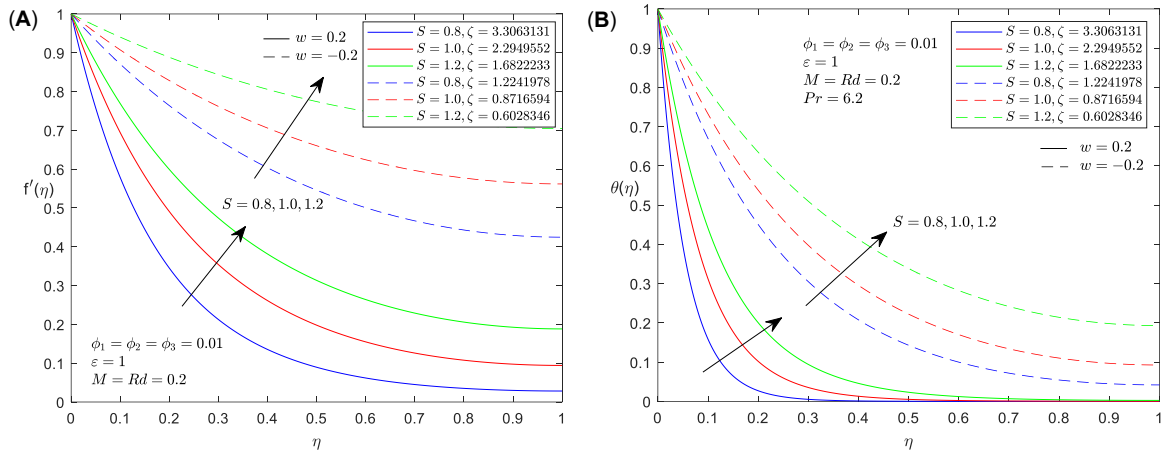

Figure 3. Variation in velocity (**A**) and temperature (**B**) profiles for different unsteady parameter S

The effects of suction $(w > 0)$ and injection $(w < 0)$ on the velocity $f'(\eta)$ and temperature $\theta(\eta)$ profiles for $S = 0.8$, $M = Rd = 0.2$ and $\varepsilon = 1$ are illustrated in Figure 4(a)-(b). The results for $w = 0$ (without suction or injection) are also included. As w increases (from 0 to 0.1 to 0.2), the velocity profiles show a significant increase in fluid velocity. Suction removes fluid from the boundary layer, leading to a thinner boundary layer and a steeper velocity gradient near the surface, which results in higher fluid velocity. Conversely, as w decreases (from 0 to -0.1 to -0.2), the velocity profiles show a notable decrease in fluid velocity. Injections introduce fluid into the boundary layer, causing an increase in boundary layer thickness and a reduction in the velocity gradient at the surface, which results in lower fluid velocity. The temperature profiles also show a decrease in temperature as w increases, as depicted in Figure 4(b). This temperature drop occurs due to the removal of heated fluid from the boundary layer by suction. Injection, on the other hand, adds fluid to the boundary layer, which may either introduce hotter fluid or decrease the heat transfer rate, resulting in a higher temperature. The thickness of the thin film ζ increases as the parameter w rises from -0.2 to 0.2. This indicates that suction leads to a thicker fluid film, while injection results in a thinner fluid film. The observed behavior suggests that the film thickness ζ is significantly affected by the type of wall transpiration, with suction promoting fluid accumulation and injection diminishing it.

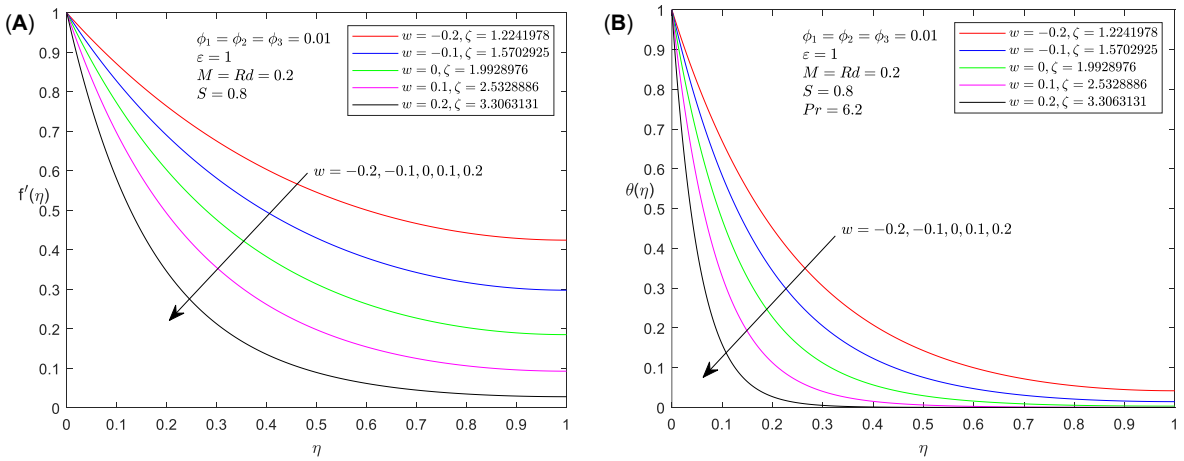

Figure 4. Variation in velocity (**A**) and temperature (**B**) profiles for different suction/injection parameter w

In Figure 5(a-b), it is clear that the velocity $f'(\eta)$ and temperature $\theta(\eta)$ profiles of ternary nanoparticles are affected by the Magnetic field parameter M. When an electrically conducting fluid flows through a magnetic field, it experiences a resistive force known as the Lorentz force, which acts to reduce the fluid's speed. As the value of the magnetic field M increases, the flow retardation becomes more significant. This slowdown leads to a thickening of the momentum boundary layer, as illustrated in Figure 5(a). In Figure 5(b), we can see that the temperature profile $\theta(\eta)$ rise as the magnetic field

strength increases. This rise is expected due to the magnetic field's effects. The Lorentz force causes the fluid to decelerate, converting kinetic energy into thermal energy, which in turn raises the temperature within the boundary layer.

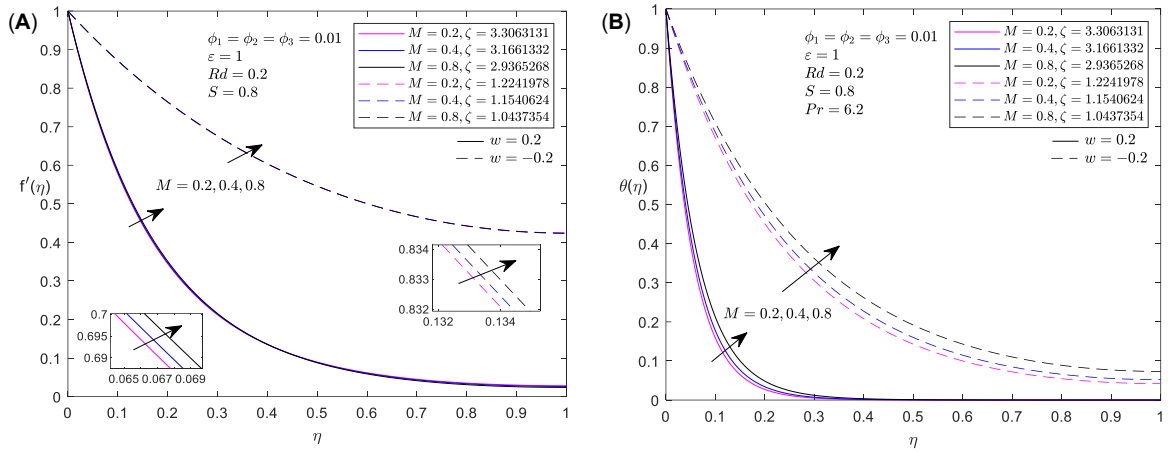

Figure 5. Variation in velocity (**A**) and temperature (**B**) profiles for different magnetic parameter M

As the stretching parameter ε increases from 1 to 2, the velocity profile $f'(\eta)$ improves near the surface, as illustrated in Figure 6(a). At larger values of η, a crossover effect is observed in the velocity profiles, suggesting a change in the ratio of viscous to inertial forces. In this context, ε signifies the rate at which the surface is stretched, with larger values of ε reflecting a quicker stretching action. This additional stretching facilitates greater momentum transfer to the fluid, leading to increased velocity. Furthermore, suction produces larger velocities closer to the boundary than injection, demonstrating the influence of wall transpiration. Increased stretching rates contribute to a thicker fluid layer, as shown by the relationship between ε and ζ. This behavior is anticipated because a rapidly stretched surface draws in more fluid, thereby increasing the film thickness. Figure 6(b) shows that raising ε leads to a reduction in the temperature profile $\theta(\eta)$, indicating improved convective heat transfer due to the heightened stretching rate, along with a corresponding rise in ζ.

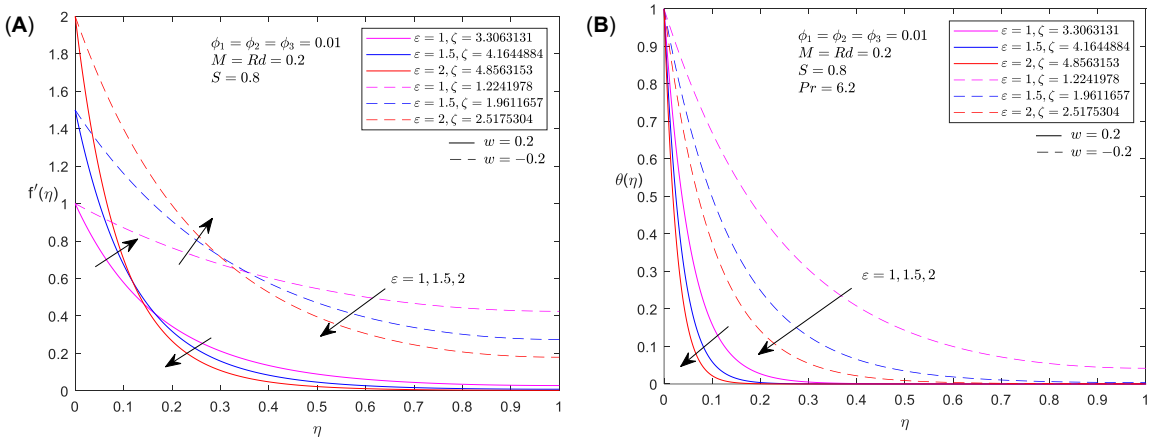

Figure 6. Variation in velocity (**A**) and temperature (**B**) profiles for different stretching parameter ε

Figure 7 depicts the effect of the radiation parameter Rd on the temperature profile $\theta(\eta)$. Increases in the radiation parameter Rd tend to enhance the fluid's temperature profile. In a ternary nanofluid system, the radiation parameter Rd assesses the importance of radiative heat transfer in relation to other modes of heat transmission such as conduction and convection. As the radiation parameter Rd increases, the ternary nanofluid system absorbs more heat radiation from outside or inside the system. The absorbed radiation elevates the temperature of the nanofluid while also contributing to the system's overall energy balance. Strong radiation heat transfer increases the rate of energy transfer into the fluid. Consequently, the temperature rises.

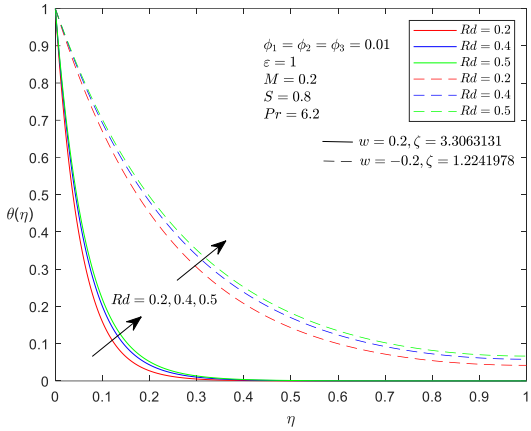

Figure 7. Temperature profiles for different Radiation parameter Rd

Table 7 present the impact of different parameter such as ϕ_3, Rd, S, M and ε on local skin friction, $C_f \mathrm{Re}_x^{1/2}$ and Nusselt number, $Nu_x \mathrm{Re}_x^{-1/2}$ for both suction $(w = 0.2)$ and injection $(w = -0.2)$ cases from Equation (14). We can see that as the value of nanoparticle volume fraction, ϕ_3 increases, the value of local skin friction and Nusselt number for both suction and injection decreasing and increases, respectively. For increasing value of Rd, only Nusselt number increasing for both cases and does not affect the local skin friction. Furthermore, when the value of unsteadiness parameter S increase, the value of local skin friction increasing for both cases while the value of Nusselt number for suction is decreasing and increasing for injection case, respectively. As the value of magnetic parameter M increase, the value of local skin friction for both cases decreases and the value of Nusselt number in suction case are decreasing while the value of Nusselt number in injection is increasing. Lastly, when the value of stretching parameter ε increase, the value of local skin friction for both cases is decreasing and the value of Nusselt number for both cases is increasing.

Table 7. Local Skin Friction, $C_f \mathrm{Re}_x^{1/2}$ and Nusselt number, $Nu_x \mathrm{Re}_x^{-1/2}$ for suction and injection cases

					$C_f \mathrm{Re}_x^{1/2}$		$Nu_x \mathrm{Re}_x^{-1/2}$	
					Suction	**Injection**	**Suction**	**Injection**
ϕ_3	Rd	S	M	ε	$w = 0.2$	$w = -0.2$	$w = 0.2$	$w = -0.2$
0	0.2	0.8	0.2	1	-1.7700339	-1.2027125	7.4859604	4.3159023
0.005					-1.8027120	-1.2245855	7.4924716	4.3450597
0.01					-1.8355412	-1.2465697	7.5001219	4.3741315
	0.4				-1.8355412	-1.2465697	7.9107124	4.8308572
	0.5				-1.8355412	-1.2465697	8.1025013	5.0431406
	0.2	1.0			-1.7582104	-1.2380483	6.8504132	4.7763567
		1.2			-1.7238481	-1.1414775	6.5706076	5.0888288
		0.8	0.4		-1.8926798	-1.3180010	7.3678224	4.3979958
			0.8		-2.0034528	-1.4502877	7.1501586	4.4309802
			0.2	1.5	-3.2070093	-2.1540775	9.0123076	4.7608826
				2	-4.7986936	-3.1231849	10.2893855	5.1682780

3.3. Response Surface Optimization

ANOVA was performed to analyze whether the variables have a significant effect $(p \le 0.05)$ on dependent variables as shown in Table 8. The Minitab 15 statistical software was used to establish the ability of the final model by means of graphical and numerical analysis. The F-values of the developed model for local Nusselt number was found to be 1345768.65 with corresponding P-values less than 0.05. This indicates that the model is significant and can be used for further analyses and optimizations. The model's P-value was less than 0.05 which indicates that it was statistically significant. However, the term $x_1 * x_1$ is insignificant variables due to the high p-value. The insignificant variable identified in Table 8 was removed from the model and excluded from the optimization study of local Nusselt number. Therefore, Table 9 summarizes the reduced quadratic model.

Table 8. Analysis of variance (ANOVA) result

Source	DF	Adj SS	Adj MS	F-value	P-value
Model	9	22.9637	2.5515	1345768.65	0.000
Linear	3	22.8560	7.6187	4018379.72	0.000
x_1	1	0.0002	0.0002	93.64	0.000
x_2	1	20.8877	20.8877	11016963.56	0.000
x_3	1	1.9682	1.9682	1038081.96	0.000
Square	3	0.0876	0.0292	15400.20	0.000
$x_1 * x_1$	1	0.0000	0.0000	0.82	0.386
$x_2 * x_2$	1	0.0395	0.0395	20817.24	0.000
$x_3 * x_3$	1	0.0011	0.0011	585.63	0.000
2-Way Interaction	3	0.0201	0.0067	3526.01	0.000
$x_1 * x_2$	1	0.0000	0.0000	14.59	0.003
$x_1 * x_3$	1	0.0000	0.0000	23.48	0.001
$x_2 * x_3$	1	0.0200	0.0200	10539.98	0.000
Error	10	0.0000	0.0000		
Lack-of-Fit	5	0.0000	0.0000	*	*
Pure Error	5	0.0000	0.0000		
Total	19	22.9637			

Table 9. Analysis of variance (ANOVA) result for the reduced model

Source	DF	Adj SS	Adj MS	F-value	P-value
Model	8	22.9637	2.8705	1538937.71	0.000
Linear	3	22.8560	7.6187	4084596.07	0.000
x_1	1	0.0002	0.0002	95.18	0.000
x_2	1	20.8877	20.8877	11198505.16	0.000
x_3	1	1.9682	1.9682	1055187.86	0.000
Square	2	0.0876	0.0438	23480.54	0.000
$x_2 * x_2$	1	0.0457	0.0457	24506.98	0.000
$x_3 * x_3$	1	0.0013	0.0013	673.37	0.000
2-Way Interaction	3	0.0201	0.0067	3584.12	0.000
$x_1 * x_2$	1	0.0000	0.0000	14.83	0.003
$x_1 * x_3$	1	0.0000	0.0000	23.86	0.000
$x_2 * x_3$	1	0.0200	0.0200	10713.66	0.000
Error	11	0.0000	0.0000		
Lack-of-Fit	6	0.0000	0.0000	*	*
Pure Error	5	0.0000	0.0000		
Total	19	22.9637			

After eliminating insignificant terms, the final regression model for $Nu_x \mathrm{Re}_x^{-1/2}$ is written as:

$$Y = 9.47788 + 0.004214\, x_1 + 1.44526\, x_2 + 0.443639\, x_3 - 0.119518\, x_2 * x_2 - 0.019811\, x_3 * x_3 - 0.001860\, x_1 * x_2 - 0.002359\, x_1 * x_3 + 0.049979\, x_2 * x_3 \quad (16)$$

The contour and surface plots in Figures 8 - 10 visually illustrate the impact of Alumina nanoparticle volume fraction (x_1), stretching rate (x_2), and radiation effect (x_3) on local Nusselt number (Response). Figure 8 illustrates the influence of the Alumina nanoparticle and stretching rate parameters on the non-dimensional local Nusselt number for $x_3 = 0$ ($Rd = 0.4$). The results indicate that the stretching rate parameter is the dominant factor influencing the heat transfer rate, meanwhile heat transfer rate appears to be relatively insensitive to changes in the Alumina nanoparticle. Figure 9 presents the interaction effects of alumina nanoparticle concentration and radiation parameter on the heat transfer rate, with the stretching rate held constant ($\varepsilon = 1.5$). The findings confirm that variations in Alumina nanoparticle concentration have little to no effect on the heat transfer rate. The heat transfer rate can be improved by independently increasing either the stretching rate or the radiation parameter, within the tested ranges, while maintaining the alumina nanoparticle concentration ($\phi_3 = 0.015$) as shown in Figure 10.

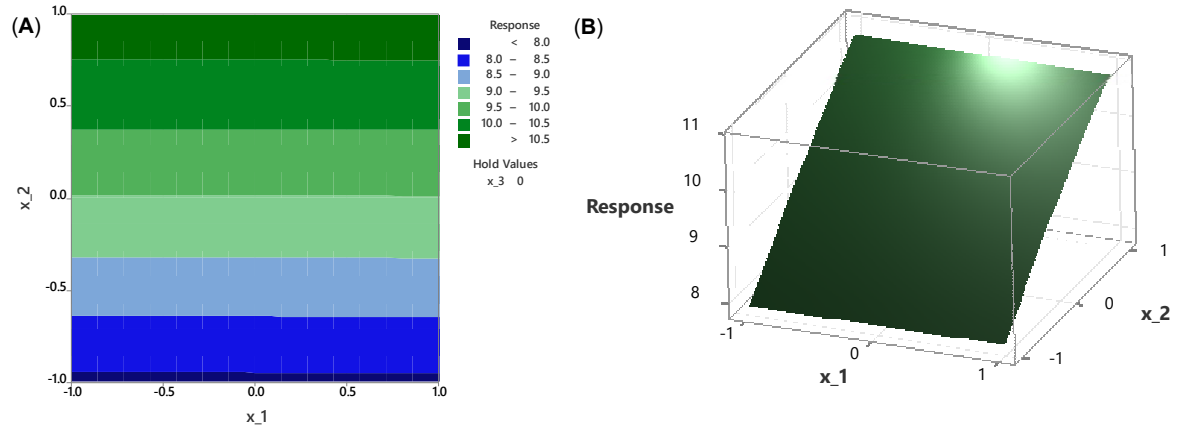

Figure 8. Variation in contour (**A**) and surface (**B**) plot for the interaction of x_1 and x_2

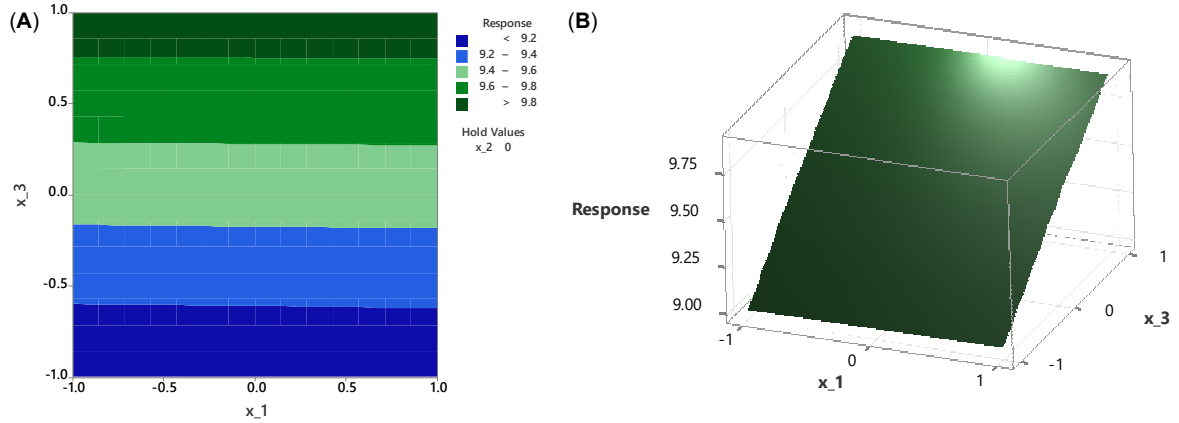

Figure 9. Variation in contour (**A**) and surface (**B**) plot for the interaction of x_1 and x_3

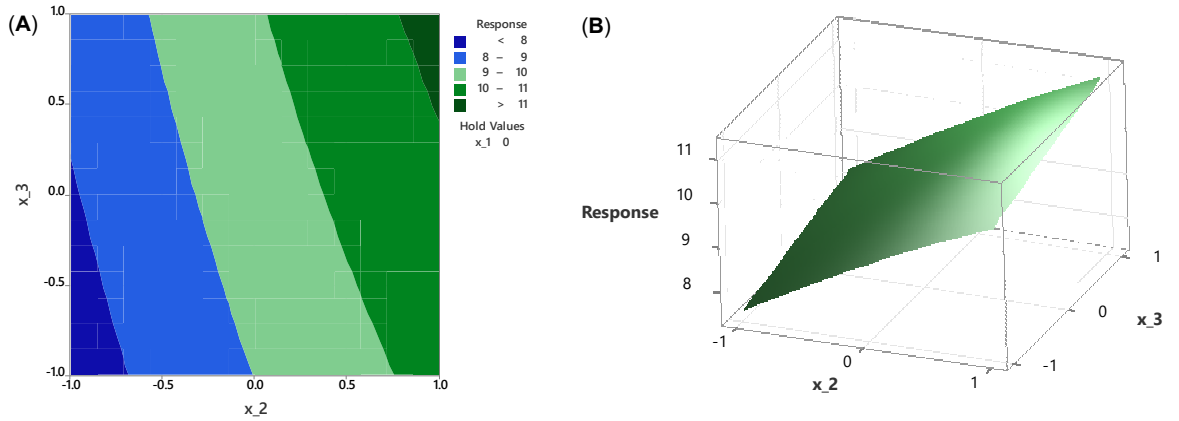

Figure 10. Variation in contour (**A**) and surface (**B**) plot for the interaction of x_2 and x_3

By utilizing the response optimizer, the optimization results show that the maximum heat transfer rate of 11.2774 is achieved at the coded levels $x_1 = -1$, $x_2 = 1$ and $x_3 = 1$ with a composite desirability of 1.000. This indicates that the selected combination of parameters provides the most favorable condition for enhancing the heat transfer rate. The rate of heat transfer is maximized when ε and Rd reach their highest values, while ϕ_3 at the lowest value achieving a composite desirability of 100%.

4. CONCLUSION

The study investigates the thin film flow and heat transfer of ternary nanofluid using numerical methods and Response Surface Methodology (RSM) under the influence of radiation effects. The model is formulated with key variables, including the magnetic parameter, nanoparticle volume fractions, thin

film thickness, suction/injection, unsteady, stretching and radiation parameters, all in dimensionless form. The similarity equations, expressed as non-dimensional ordinary differential equations, are solved using the similarity variables method. The bvp4c function in MATLAB is utilized to numerically compute the first-order ODE system. Based on the mathematical model and numerical experiment data, the heat transfer coefficients are statistically optimized in Minitab. The optimization procedure incorporates three key parameters and involves twenty simulation runs. The results indicate that the velocity field was dramatically reduced due to the influence of the Alumina nanoparticle fraction and suction/injection parameter while it was augmented with positive variation radiation, unsteady and magnetic parameter. The temperature profile was boosted under the effects of radiation, unsteady, magnetic field and nanoparticle volume fraction. Thin film thickness affects all parameters except radiation, which mainly influences energy exchange without changing the film's structure. The RSM optimization confirms that higher stretching and radiation effects, lower Alumina nanoparticle levels are essential for maximizing heat transfer.

ACKNOWLEDGEMENT
Authors acknowledge the Ministry of Higher Education (MOHE) for funding under the Geran Penyelidikan Fundamental Penyelidik Muda - Early Career Researcher (FRGS-EC/1/2024/STG06/UITM/02/13).

CONFLICT OF INTEREST
The authors declare no conflicts of interest.

AUTHOR CONTRIBUTION
Nur Syazana Anuar: Conceptualization, Methodology, Formal Analysis and Writing original draft. Al-Nurul Amni Athirah Hasbullah: Formal analysis, Validation and Writing. Nur Adilah Liyana Aladdin: Methodology, Investigation, Reviewing and Editing. Norfifah Bachok: Supervision, Reviewing and Editing. Zeeshan Khan: Project Administration, Reviewing and Editing.

DATA AVAILABILITY
All data generated or analyzed during this study are included in this published article.

DECLARATION OF GENERATIVE AI
Not applicable.

ETHICS
Not applicable.

REFERENCES

Alharbi AF, Alhawiti M, Usman M, Ullah I, Alam MM, Bilal M. (2024). Enhancement of heat transfer in thin-film flow of a hybrid nanofluid over an inclined rotating disk subject to thermal radiation and viscous dissipation. *International Journal of Heat and Fluid Flow*, 107, 109360. doi:10.1016/j.ijheatfluidflow.2024.109360

Alraddadi I, Ayub A, Hussain SM, Khan U, Shah SZH, Hassan AM. (2023). The significance of ternary hybrid cross bio-nanofluid model in expanding/contracting cylinder with inclined magnetic field. *Frontiers in Materials*, 10, 1242085. doi:10.3389/fmats.2023.1242085

Bhattacharya A, Calmidi VV, Mahajan RL. (2002). Thermophysical properties of high porosity metal foams. *International Journal of Heat and Mass Transfer*, 45(5), 1017-1031. doi:10.1016/S0017-9310(01)00220-4

Bilal M, Ullah I, Alam MM, Weera W, Galal AM. (2022). Numerical simulations through PCM for the dynamics of thermal enhancement in ternary MHD hybrid nanofluid flow over plane sheet, cone, and wedge. *Symmetry*, 14(11), 2419. doi:10.3390/sym14112419

Das K, Acharya N, Kundu PK. (2017). Thin film flow over an unsteady stretching sheet with thermocapillarity in presence of magnetic field. *Thermal Science*, 21, 2369-2378. doi:10.2298/TSCI150221141D

Gomathy G, Kumar BR. (2024). Impacts of nanoparticle shapes on Ag-water nanofluid thin film flow through a porous medium with thermal radiation and ohmic heating. *Journal of Thermal Analysis & Calorimetry*, 149(13). doi:10.1007/s10973-023-12609-z

Gull L, Mushtaq A, Mehmood T, Mustafa M. (2024). Exploring slip flow of viscoelastic fluid with frictional heating effects: Uncertainty analysis using response surface methodology (RSM). *International Communications in Heat and Mass Transfer*, 155, 107548. doi:10.1016/j.icheatmasstransfer.2024.107548

Hayat U, Shaiq S, Shahzad A. (2025). Numerical investigation and analysis of heat transfer and thin film flow of Fe_3O_4 and Al_2O_3 nanoparticles dispersed in H_2O over vertical stretching sheet. *Numerical Heat Transfer, Part A: Applications*, 86(9), 2778-2792. doi:10.1080/10407782.2023.2294054

Haq F, Ghazwani HA, Younis J, Ghazwani MH, Alnujaie A. (2025). Numerical investigation of mass and heat transfer in ternary hybrid nanofluid flow with activation energy. *International Journal of Energy Research*, 2025(1), 8061691. doi:10.1155/er/8061691

Hema S, Venkatesh P, Gireesha BJ, Pavithra CG. (2025). Flow and heat transfer analysis of MHD ternary hybrid nanofluid flow through a vertical porous microchannel with slip boundary conditions. *Multiscale and Multidisciplinary Modeling, Experiments and Design*, 8(3), 183. doi:10.1007/s41939-025-00764-9

Jamrus FN, Waini I, Khan U, Ishak A. (2024a). Effects of magnetohydrodynamics and velocity slip on mixed convective flow of thermally stratified ternary hybrid nanofluid over a stretching/shrinking sheet. *Case Studies in Thermal Engineering*, 55, 104161. doi:10.1016/j.csite.2024.104161

Jamrus FN, Ishak A, Waini I, Khan U, Siddiqui MIH, Madhukesh JK. (2024b). Aspects of non-unique solutions for hiemenz flow filled with ternary hybrid nanofluid over a stretching/shrinking sheet. *Advances in Mathematical Physics*, 1, 7253630. doi:10.1155/2024/7253630

Kamis NI, Jiann LY, Shafie S, Khairuddin TKA, Basir MFM. (2022). Magnetohydrodynamics boundary layer flow of hybrid nanofluid in a thin-film over an unsteady stretching permeable sheet. *Journal of Nanofluids*, 11(1), 74-83. doi:10.1166/jon.2022.1821

Malleswari K, Sarojamma G. (2025). Unsteady thin film flow of a hybrid nanoliquid with magnetic effects. *World Journal of Engineering*, 22(4), 749-759. doi:10.1108/WJE-01-2024-0043

Mathew A, Areekara S, Sabu AS. (2021). Sensitivity analysis on radiative heat transfer of hydromagnetic Carreau nanoliquid flow over an elongating cylinder using Bulirsch-Stoer algorithm. *Thermal Science and Engineering Progress*, 25, 101038. doi:10.1016/j.tsep.2021.101038

Montgomery DC. (2017). Design and analysis of experiments. John Wiley & Sons.

Mukhtar S, Gul T. (2023). Solar radiation and thermal convection of hybrid nanofluids for the optimization of solar collector. *Mathematics*, 11(5), 1175. doi:10.3390/math11051175

Noor NFM, Abdulaziz O, Hashim I. (2010). MHD flow and heat transfer in a thin liquid film on an unsteady stretching sheet by the homotopy analysis method. *International Journal for Numerical Methods in Fluids*, 63(3), 357-373. doi:10.1002/fld.2078

O'brien SBG, Schwartz LW. (2002). Theory and modeling of thin film flows. *Encyclopedia of Surface and Colloid Science*, 1, 5283-5297.

Puneeth V, Manjunatha S, Makinde OD, Gireesha BJ. (2021). Bioconvection of a radiating hybrid nanofluid past a thin needle in the presence of heterogeneous–homogeneous chemical reaction. *Journal of Heat Transfer*, 143(4), 042502. doi:10.1115/1.4049844

Pyari DR, Thumma T, Ontela S. (2025). Comparative analysis of response surface methodology and sensitivity analysis on radiative hybrid nanofluid flow over an inclined spinning disk with non-uniform heat source. *Multiscale and Multidisciplinary Modeling, Experiments and Design*, 8(3), 162. doi:10.1007/s41939-025-00742-1

Ramesh GK, Madhukesh JK, Das R, Shah NA, Yook SJ. (2025). Thermodynamic activity of a ternary nanofluid flow passing through a permeable slipped surface with heat source and sink. *Waves in Random and Complex Media*, 35(2), 3499-3519. doi:10.1080/17455030.2022.2053237

Reddy YD, Mebarek-Oudina F, Goud BS, Ismail AI. (2022). Radiation, velocity and thermal slips effect toward MHD boundary layer flow through heat and mass transport of Williamson nanofluid with porous medium. *Arabian Journal for Science and Engineering*, 47(12), 16355-16369. doi:10.1007/s13369-022-06825-2

Reddy YD, Mangamma I. (2023). Influence of velocity slip and viscous dissipation on MHD heat transfer Fe3O4-ethylene glycol nanofluid flow over a shrinking sheet with thermal radiation. *Journal of Computational Biophysics and Chemistry*, 22(7), 815-828. doi:10.1142/S2737416523500424

Samat NAA, Bachok N, Arifin NM. (2024). Boundary layer stagnation point flow and heat transfer over a nonlinear stretching/shrinking sheet in hybrid carbon nanotubes: numerical analysis and response surface methodology under the influence of magnetohydrodynamics. *Computation*, 12(3), 46. doi:10.3390/computation12030046

Sharma D, Sood S, Thakur A, Prasad S. (2023). Numerical Analysis of Williamson-Micropolar Ternary Nanofluid Flow Through Porous Rotatory Surface. *Journal of Nanofluids*, 12(8), 2234-2344. doi:10.1166/jon.2023.2092

Wang CY. (1990). Liquid film on an unsteady stretching surface. *Quarterly of Applied Mathematics*, 48(4), 601-610. doi:10.1090/qam/1079908

Wang C. (2006). Analytic solutions for a liquid film on an unsteady stretching surface. *Heat and Mass Transfer*, 42(8), 759-766. doi:10.1007/s00231-005-0027-0

Wahid NS, Mustafa MS, Arifin NM, Pop I, Anuar NS, Khashi'ie NS. (2024). Numerical and statistical analyses of three-dimensional non-axisymmetric Homann's stagnation-point flow of nanofluids over a shrinking surface. *Chinese Journal of Physics*, 89, 1555-1570. doi:10.1016/j.cjph.2023.11.034

Wahid NS, Mustafa MS, Arifin NM, Khashi'ie NS, Pop I. (2025). Hybrid nanofluid radiative flow across a permeable convective moving surface with heat generation: numerical and statistical approach. *Neural Computing and Applications*, 37(5), 2911-2923. doi:10.1007/s00521-024-10834-7

Zeeshan, Khan I, Weera W, Mohamed A. (2022). Heat transfer analysis of Cu and Al2O3 dispersed in ethylene glycol as a base fluid over a stretchable permeable sheet of MHD thin-film flow. *Scientific Reports*, 12(1), 8878. doi:10.1038/s41598-022-12671-x